Received: 3 November 2022 | Accepted: 9 November 2022

DOI: 10.1002/nano.202200200

RESEARCH ARTICLE

Nano Select Open Access WILEY

Mg/Zn metal-air primary batteries using silk fibroin-ionic liquid polymer electrolytes

Mathew J. Haskew[1,2] | **Shahin Nikman**[2] | **Carys E. O'Sullivan**[2] | **Hanaa A. Galeb**[2,3] | **Nathan R. Halcovitch**[2] | **John G. Hardy**[2,4] | **Samuel T. Murphy**[1,4]

[1]School of Engineering, Lancaster University, Bailrigg, Lancaster, UK

[2]Department of Chemistry, Lancaster University, Faraday Building, Bailrigg, Lancaster, UK

[3]Department of Chemistry, Science and Arts College, Rabigh Campus, King Abdulaziz University, Jeddah, Saudi Arabia

[4]Materials Science Institute, Lancaster University, Faraday Building, John Creed Avenue, Bailrigg, Lancaster, UK

Correspondence
John G. Hardy, Department of Chemistry, Lancaster University, Faraday Building, John Creed Avenue, Bailrigg, Lancaster LA1 4YB, UK.
Email: j.g.hardy@lancaster.ac.uk
Samuel T. Murphy, School of Engineering, Lancaster University, Bailrigg, Lancaster, UK.
Email: samuel.murphy@lancaster.ac.uk

Abstract

Batteries are utilized in a multitude of devices encountered in our daily lives. Here we describe a comparative study of Magnesium-air and Zinc-air primary batteries using silk fibroin-ionic liquid polymer electrolytes (composed of *Bombyx mori* silk fibroin and choline nitrate). The ionic conductivity of the films was of the order of mS cm^{-1} which is sufficient to satisfy the conductivity requirements for many battery applications, the open circuit voltages (V) for the Mg 1:1 SF:IL and 1:3 SF:IL batteries just after fabrication were ca. 1.8 and 1.7 V, respectively; the 1:1 SF:IL battery had a capacity of 0.84 mAh cm^{-2}, whereas the 1:3 SF:IL battery had a capacity of 0.68 mAh cm^{-2}. The open circuit voltages (V) for the Zn 1:1 SF:IL and 1:3 SF:IL batteries were in the range of 1.3 and 1.2 V just after fabrication; the 1:3 SF:IL battery displayed a capacity of 0.96 mAh cm^{-2} and the 1:3 SF:IL battery displayed a capacity of 0.72 mAh cm^{-2}. Integration of the PE and substitution of the carbon cloth electrodes with degradable materials would offer routes to production of transient primary batteries helping to address the global issue of electronic waste (e-waste).

KEYWORDS
batteries, electronics, ionic liquids, polymer electrolytes, silk fibroin

1 | INTRODUCTION

Electronic devices are ubiquitous in our lives, as is the generation of waste (in this case electronics waste, e-waste) resulting from the production and eventual disposal after the product has reached the end of its useful lifetime. There are more than 50 million tonnes of e-waste discarded annually (worth in excess of $60B),[1–5] which increases annually in accordance with global population growth, global efforts to reduce poverty (e.g., via the 17 United Nations Sustainable Development Goals),[6] and increasing use of electronic devices in our lives. The potential hazards associated with some of the components of e-waste (e.g., ecological concerns include air/soil/water pollution) make it an issue of global importance.[7] Consequently, the development of electronics employing a circular economy perspective is important, involving: natural/materials scientists/engineers involved in the design and manufacture of electronics, and people involved in the primary/secondary/tertiary/quaternary/quinary industry sectors.[8–11] While there are initiatives to develop products within a circular economy, reusing items where possible,

reducing the amounts of waste produced, and recycling waste streams across the world, the world's complex geopolitics make e-waste a global challenge.

Batteries are used to store energy for use on demand by technologies that we use on a daily basis across the world. Primary batteries (e.g., those used for low-drain applications including electronic keys, pacemakers, remote controls, sensors, etc.) cannot be recharged, whereas secondary batteries (e.g., those used for cars, laptops, phones, etc.) are rechargeable.[12–14] Their importance in our lives underpins the reason they are the focus of significant research and development in academic and industry settings worldwide, to address issues including cost, charging speeds, safety, supply chain issues, etc.[15]

Metal-air batteries have received much attention recently because of their properties.[16] For instance, Mg-air batteries possess a high theoretical volumetric capacity of 3833 mAh cm^{-3} and low reduction potential of −2.37 V versus the standard hydrogen electrode (SHE)[17]; a theoretical energy density of 6.80 kW h kg^{-1},[18,19] and Mg^{2+} ions are abundant in the body.[20] However, Mg-air batteries can suffer from high polarization and low coulombic efficiency, typically caused by corrosion arising from the reaction of Mg and the electrolyte and the sluggish kinetics of the oxygen reduction reaction (ORR) on the cathode (often Pt)[19]; and Mg deposition and dissolution processes in polar organic electrolytes may lead to the formation of a passivation film with an insulating effect towards Mg^{2+} ions.[17] Like Mg-air batteries, Zn-air batteries have received much attention recently,[21]] because Zn possess a high theoretical volumetric capacity of 5855 mAh cm^{-3} and low reduction potential of −0.76 V versus the SHE,[22]] a theoretical energy density of 1.65 kW h kg^{-1},[22] and Zn is an essential nutrient,[21] suggest it may prove useful as a biocompatible and biodegradable metal alongside Mg.[17] However, Zn-air batteries can also suffer from issues such as, passivation, dendrite growth, and hydrogen evolution from the hydrogen evolution reaction (HER) during the use of the battery, limiting the practical applications by weakening the discharge performance of Zn-air batteries.[23,24]

Degradable/transient electronics that could be disposed of safely in the environment after use, or indeed inside a body if used for medical purposes for human/veterinary applications, are an exciting class of electronic materials,[25–31] and degradable polymers can be useful components in the development of such degradable/transient electronics.[32–38] Degradable batteries/capacitors are an area of current research interest for their potential economic, environmental, and health impacts.[27,39,40–42] By comparison with the vast literature on traditional batteries,[12] there are relatively few examples of transient batteries in the literature due to challenges related to the fact that they must fulfill very different requirements than for traditional batteries (e.g., solid-state electrolytes such as polymer electrolytes, PEs, may not be conductive enough)[43–45]; and this exciting area of science and engineering has attracted the attention of researchers from various disciplines investigating various feedstocks for components of degradable batteries (i.e., anodes, cathodes, electrolytes, and containers) including: peptides,[46] polysaccharides,[47–49] synthetic polymers (e.g., polycaprolactone,[50] poly(glycerol sebacate),[51] ionic liquids,[52,53] with examples of batteries that are metal containing[54–58] or indeed metal free.[40]

Natural/engineered silk proteins (such as *Bombyx mori* silk fibroin) are a class of degradable polymers that have potential for application in electronics.[1,59,60–67] SF from the *B. mori* silkworm is a protein that has been investigated for various technical and biomedical applications (including textiles, sutures, drug delivery devices, tissue scaffolds, etc.), and SF-based materials have potential for use as components of transient electronic devices (e.g., encapsulants, PEs, substrates, etc.).[68–75] Ionic liquids are appealing when developing safe (i.e., non-flammable) energy storage devices (e.g., batteries and capacitors) due to their tunable properties (e.g., acidity/basicity, electrochemical windows, polarity) combined with generally high thermal stability, low volatility/flammability, high ionic conductivity.[76–81] Ionic liquids have been used as solvents for proteins for fundamental and applied research,[82–90] including various silk proteins.[61,91–99] Pioneering work has employed the combination of ionic liquids and silk proteins to generate materials for energy storage applications, including batteries[59,100] and capacitors.[101–103]

This study builds upon the exciting examples of combining silks and ionic liquids for energy storage,[59,100] by comparing metal-air primary batteries employing Mg/Zn, *B. mori* SF, and a choline-based ionic liquid (choline nitrate).[74] Mg-air (employing the alloy Mg AZ31) or Zn-air[59,104] batteries, utilizing a PE composite consisting of *B. mori* SF and an ionic liquid (IL), [Ch][NO_3],[105] wherein the SF immobilizes the IL creating an ion conducting separator between the electrodes. The efficiency of the PEs was demonstrated when deployed in the batteries and their discharge profiles were evaluated.

2 | RESULTS AND DISCUSSION

2.1 | Polymer electrolyte and battery preparation

The PE films that serve as the ion conducting separator between the two electrode terminals for the primary batteries have previously been reported in the literature (and

are composed of a combination of the polymer SF and IL electrolyte, at either a 1:1 or 1:3 wt. ratio of SF:IL [chosen as they are functional and handleable], as previously reported in the literature).[44,59,64,74] The ionic liquid (IL, choline nitrate, [Ch][NO_3]) was prepared via the neutralization of nitric acid with choline hydroxide, in accordance with the literature.[2553,74,105] Fourier-transform infrared (FTIR) spectroscopy and X-ray diffraction (XRD) were used to analyze the components of the PE in their aqueous solution state and solid (film) state. FTIR data (IL Figure S1, SF Figure S2, PE with a 1:1 wt. ratio of SF:IL Figure S3 and PE with a 1:3 wt. ratio of SF:IL Figure S4) was in line with that reported in the literature: peaks at 1330 cm^{-1} from the NO_3^- and 954 cm^{-1} from the C-C-OH, were characteristic of the IL[59]; and peaks observed at ca. 1690 cm^{-1} amide I (characteristic of β-turns), 1625 cm^{-1} amide I (characteristic of β-sheets), ca. 1550 cm^{-1} amide II (unordered), 1520 cm^{-1} Tyr-OH, ca. 1510 cm^{-1} amide II (β-sheets), ca. 1313 cm^{-1} amide III (β-turns), ca. 1219 cm^{-1} amide III (β-sheets), were characteristic of *B. mori* SF[106]; interestingly, the FTIR data for the *B. mori* SF is indicative of the presence of both silk I (a β-turn type II conformation-rich structure) and silk II (silk II is an antiparallel β-sheet-rich structure) structures in the silk and PE films.[107,108] XRD data (Figure S5) of the solution state PE with a 1:1 wt. ratio of SF:IL, solid state PE with a 1:1 wt. ratio of SF:IL, solution state PE with a 1:3 wt. ratio of SF:IL, and solid state PE with a 1:3 wt. ratio of SF:IL) are all very broad indicative of amorphous unordered structures. Untreated SF films exhibit a broad peak at 20° 2-θ which is a typical characteristic pattern of an amorphous silk material[109–111]; for samples with a 1:1 wt. ratio of SF:IL the diffractograms have a broad peak at ca. 8° 2-θ (amorphous, silk I) and a peak at ca. 13° 2-θ (β-turn, silk I), whereas the diffractograms of the samples with a 1:3 wt. ratio of SF:IL only have a broad peak at ca. 8° 2-θ (amorphous, silk I) indicative of the role of the IL in dissolving the SF.[91,112] The presence of water in the films is important because of its role as a proton source to support the ORR at the cathode,[113] and thermogravimetric analysis (TGA, Figure S6) was used to determine the residual water content of the PE films (6% by weight for the 1:1 PE film and 7% by weight for the 1:3 PE film), which was similar to previously reported values for analogous PE films (mass loss below 100°C was ascribed to bulk water, whereas mass loss at ca. 125°C was ascribed to water molecules interacting with the SF, and mass loss above 200°C was due to degradation of the SF).[59] The PE films were used as ion conducting separators between the two electrode terminals for primary Mg-air or Zn-air batteries; the cathode for the ORR was a Pt black carbon cloth electrode, and the anodes were either Mg AZ31 alloy foil or Zn foil to facilitate a comparative study of the effect of changing the anode material. The battery construction/design

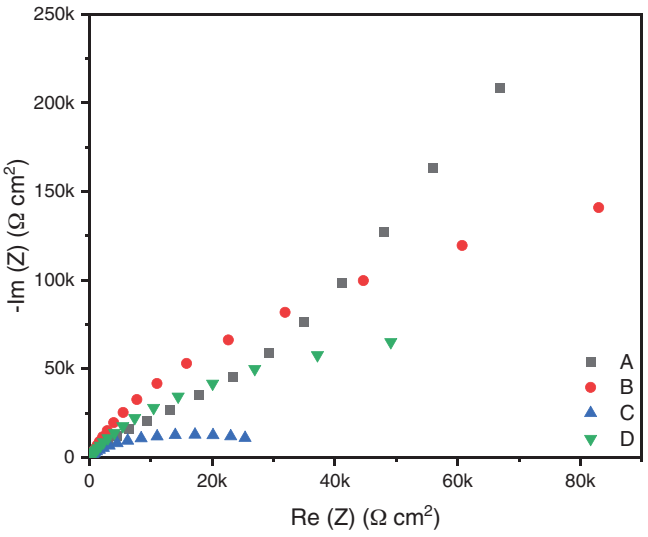

FIGURE 1 PEIS spectra. A, 1:1 PE assembled in the primary Mg-air battery. B, 1:3 PE assembled in the primary Mg-air battery. C, 1:1 PE assembled in the primary Zn-air battery. D, 1:3 PE assembled in the primary Zn-air battery

is shown in Figures S7–S9; the 1 mm drilled air holes in Figures S7 and S8 were not initially incorporated within the battery design, Figure S9, but were included to increase the amount of oxygen reaching the working components within the battery once assembled. PEIS of the systems studied resulted in the Nyquist plots (Figure 1, Figure S10) used to calculate the ionic conductivity of the films. For the 1:1 PE films this was 3.74 mS cm^{-1} for the Mg anode battery and 3.35 mS cm^{-1} for the Zn anode battery, and for the 1:3 PE films it was 4.90 mS cm^{-1} for the Mg anode battery and 7.96 mS cm^{-1} for the Zn anode battery in agreement with the literature and sufficient to satisfy the conductivity requirements for many battery applications.[59,114–116]

2.2 | Primary Mg-air batteries

The open circuit voltages (V) for the Mg 1:1 SF:IL and 1:3 SF:IL batteries just after fabrication were ca. 1.8 and 1.7 V, respectively (Figure 2, Figure S11). The cell voltage decreased immediately when a discharge current was applied, likely due to the high overpotential of ORR on the cathode side, and soon reached a plateau. At a current density of 25 μA cm^{-2} the 1:1 SF:IL battery had a capacity of 0.84 mAh cm^{-2}, whereas the 1:3 SF:IL battery had a capacity of 0.68 mAh cm^{-2}. The plateau voltages (approximately the middle point of the discharge curve) were ca. 0.9 V and ca. 0.7 V for the 1:1 SF:IL and 1:3 SF:IL batteries, respectively. The specific volumetric power density *P* of the batteries was calculated from the discharge curves in Figure 2A; the 1:1 SF:IL battery could deliver a volumetric

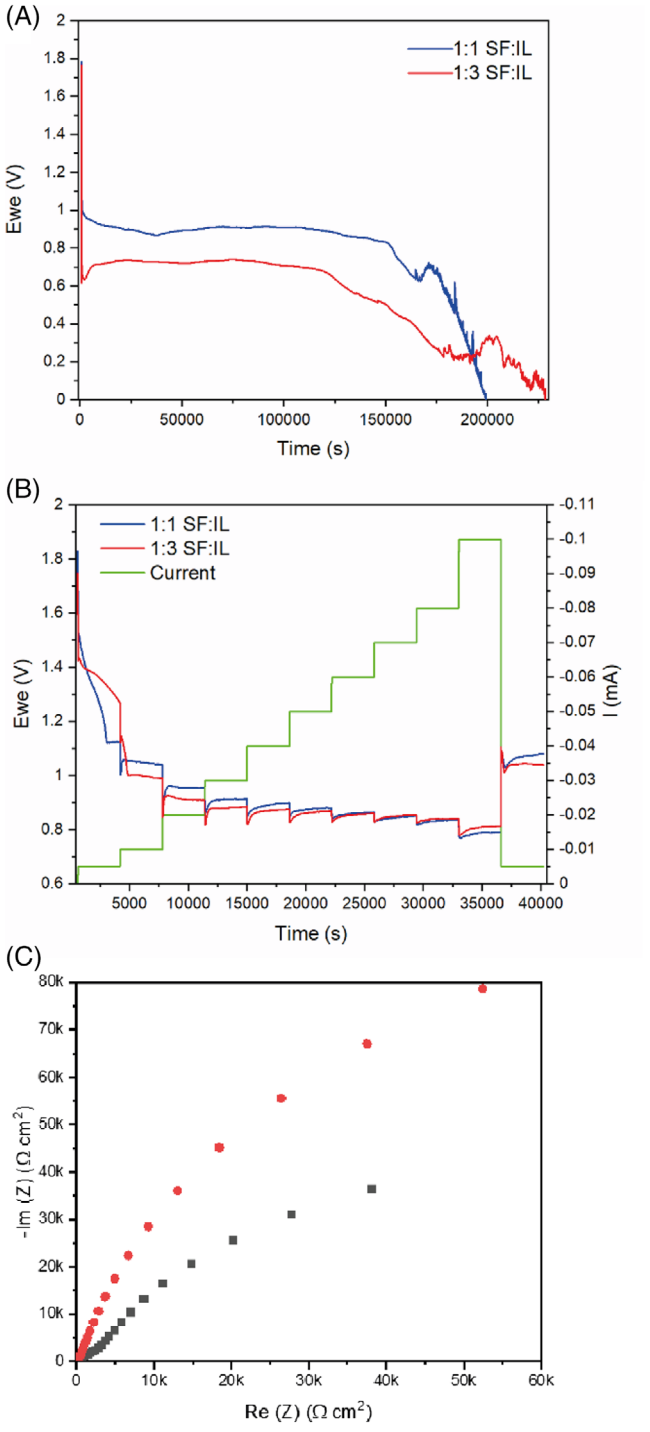

FIGURE 2 A, Discharge performance of the primary Mg-air battery using the 1:1 SF:IL PE (blue line) and the 1:3 SF:IL PE (red line) at a current density of 25 μA cm^{-2}. B, Discharge performance of the primary Mg-air battery using the 1:1 SF:IL PE (blue line) and the 1:3 SF:IL PE (red line) at varying current (green line) applied. C, PEIS spectra of the 1:1 PE assembled in the primary Mg-air battery post-discharge (black squares) and of the 1:3 PE assembled in the primary Mg-air battery post-discharge (red circles)

power density of 0.17 W L^{-1} and an energy density of 7.18 Wh L^{-1}, whereas 1:3 SF:IL battery could deliver a volumetric power density of 0.14 W L^{-1} and an energy density of 4.66 Wh L^{-1}. When compared to the literature, these batteries demonstrated similar capacities but at higher current densities. For instance, an unsealed primary Mg-air battery using nanoparticles of gold as the cathode instead of platinum and with similar electrolyte, reported a capacity of 1.43 mAh cm^{-2} at a current density of 10 μA cm^{-2}.[59] The 1:1 SF:IL and 1:3 SF:IL batteries reported here demonstrated capacities of 0.84 and 0.68 mAh cm^{-2}, respectively, at a current density of 25 μA cm^{-2}. Importantly, the power offered from the 1:1 SF:IL PE battery at 23.33 μW cm^{-2} and from the 1:3 SF:IL PE battery at 18.72 μW cm^{-2} may fulfill the requirements for the average consumption of some published implantable biomedical devices (e.g., wireless implantable sensing systems).[115,116]

To further investigate and evaluate the performance of the 1:1 and 1:3 SF:IL PEs utilized in these batteries, the averaged (from three repeated experiments) discharge performance of the batteries with varying current applied was conducted, with results displayed in Figure 2B. From Figure 2B the performance of each battery with 1:1 SF:IL or 1:3 SF:IL as electrolyte is similar within the current range of 0 to 100 μA over the timeframe of ca. 11 hours. The data in Figure 2A and 2B highlights that the main difference between 1:1 SF:IL and 1:3 SF:IL as a PE in these batteries is the capacity, with the 1:1 SF:IL PE battery possessing a slightly higher capacity. In addition, the ionic conductivity of the 1:3 SF:IL PE is greater than that of the 1:1 SF:IL PE just after battery assembly, as previously mentioned. We observed that with a higher concentration of the choline nitrate IL in the PE film, the materials are more ionically conductive (however, higher concentrations of choline nitrate IL could result in the IL separating from the PE that would impact the PEs performance within the battery).[59] The electrolyte must be able to solvate Mg/Zn ions and facilitate their transport diminishing likelihood of accumulation in the proximity of the electrode surface and precipitation as Mg/Zn salts/oxides. The ionic conductivity of the PE films post-discharge was investigated in order to compare them with the initial PEIS spectra and examine the stability of the PE films. The averaged Nyquist plot for the batteries utilizing the 1:1 SF:IL and 1:3 SF:IL composite films post-discharge are displayed in Figure 2C. The ionic conductivity of the PE composites was estimated using Equation (1) and the data from Figure 2C, finding the average ionic conductivity post-discharge for the 1:1 PE film was 3.18 mS cm^{-1}, and for the 1:3 PE film was 3.54 mS cm^{-1}. Comparing the ionic conductivity of the PE composite films before and after electrochemical experimentation, the 1:1 SF:IL PE ionic conductivity is less by a factor of

1.18, whereas the 1:3 SF:IL PE ionic conductivity is less by a factor of 1.38. Consequently, with the ionic conductivity of the 1:3 SF:IL PE decreasing more than the 1:1 SF:IL PE, it appears that the 1:3 SF:IL PE composite is less stable under the same experimental conditions (potentially because the IL from the 1:3 SF:IL PE is prone to separating due to the lower concentration of SF present and decreased capacity within the battery, as demonstrated in Figure 2A), highlighting the importance of understanding the chemistry underpinning the interactions between SF and the IL in the function of the PE composite films used in materials for energy storage.

2.3 | Primary Zn-air batteries

The assembly of the Zn-air battery was the same as that of the Mg-air battery (shown in Figure S7 and S8), with the only difference being the materials used in the anode. Before experimental measurements with the batteries (Figure 3 and Figure S12), areas of the anode foil around the PE film were secured using clear Sellotape, preventing the two terminals (anode and cathode) from contacting one another. The averaged (from three repeated experiments) discharge performance of the primary Zn-air battery, utilizing the choline nitrate IL immobilized by SF as electrolyte, is displayed in Figure 3A.

The open circuit voltages (V) for the Zn 1:1 SF:IL and 1:3 SF:IL batteries were in the range of 1.3 and 1.2 V just after fabrication. The cell voltage again decreased immediately when a discharge current was applied, likely due to the battery's internal resistance, and soon reached a plateau. The large voltage drop observed for the batteries at the start of discharge is probably due to the ORR overpotential on the Pt black carbon cloth cathode. Therefore, fabrication of future batteries could be optimized to mitigate this voltage drop from ca. 0.8 V to ca. 0.4 V, for instance, using Au nanoparticles deposited onto a SF film as the cathode.[59]

At a current density of 25 μA cm^{-2} the 1:1 SF:IL battery displayed a capacity of 0.96 mAh cm^{-2}. For the 1:3 SF:IL batteries, each discharge experiment conducted showed oscillating signals ca. 131,000 seconds or 35 hours into the experiment which were observed for varying durations, some seemingly indefinite (e.g., over 360,000 seconds or 100 hours) and others only for a couple hours after first observation. The average of the discharge experiments showing the oscillating signals are shown in Figure 3A; the capacity for the 1:3 SF:IL battery (0.72 mAh cm^{-2}) was determined using data prior to any oscillating signals are observed.

It is unclear what causes these oscillating signals in Figure 3A for the 1:3 SF:IL PE battery, because these

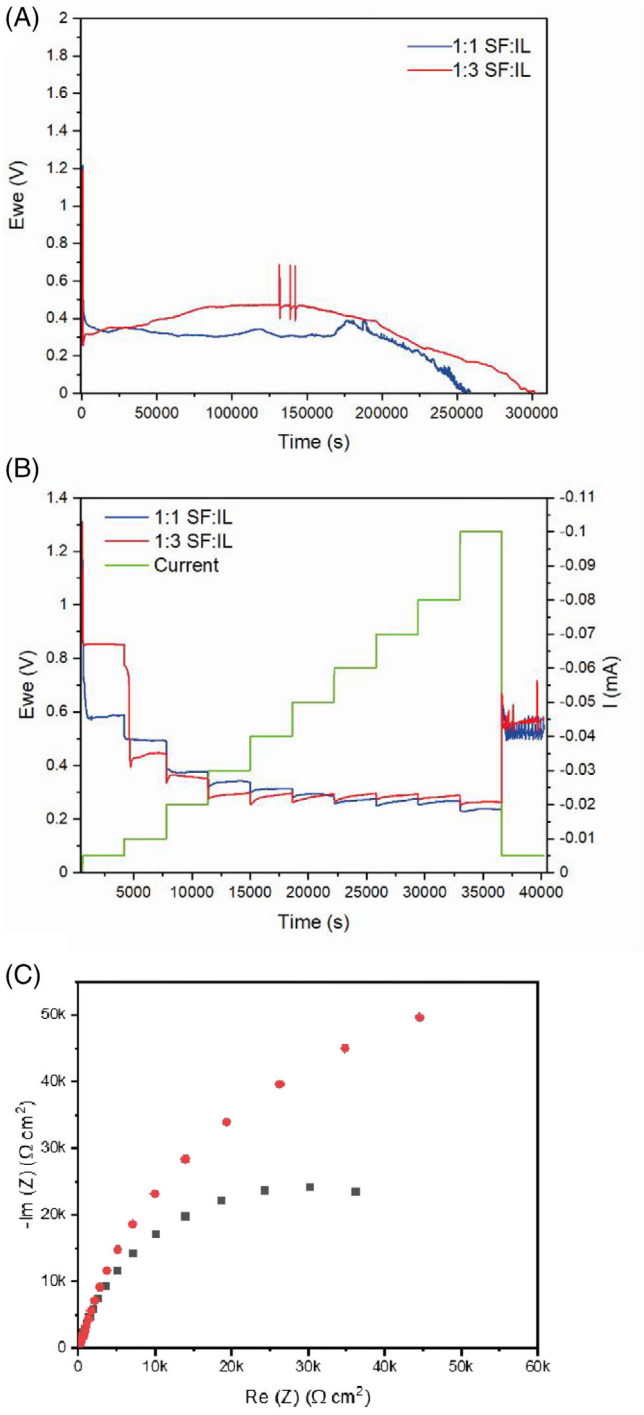

FIGURE 3 A, Discharge performance of the primary Zn-air battery using the 1:1 SF:IL PE (blue line) and the 1:3 SF:IL PE (red line) at a current density of 25 μA cm^{-2}. B, Discharge performance of the primary Zn-air battery using the 1:1 SF:IL PE (blue line) and the 1:3 SF:IL PE (red line) at varying current (green line) applied. C, PEIS spectra of the 1:1 PE assembled in the primary Zn-air battery post-discharge (black squares) and of the 1:3 PE assembled in the primary Zn-air battery post-discharge (red circles)

signals were not observed for the 1:1 SF:IL battery. However, it is plausible that this phenomenon is due to the Zn reacting with the water within the PE to form excess hydrogen which may disrupt the battery's discharge performance. The excess hydrogen potentially formed after Zn reacts with the water within the PE and its ability to escape, could explain the oscillating signals and with various time lengths observed. As aforementioned it is possible that the IL in the 1:3 SF:IL PE separates, and it has a higher water content (as observed from data displayed in Figure S6), support this prediction; future experiments to elucidate this could utilize differential electrochemical mass spectroscopy (DEMS) setup with the 1:3 SF:IL PE Zn-air battery to assess if excess hydrogen is being formed ca. 35 hours into the discharge experiment.

The specific volumetric power density (P) of the batteries were calculated following the same method first used for the Mg-air batteries, using Equation (2). The V of the SF:IL Zn-air battery is 8.697×10^{-5} L. The 1:1 SF:IL battery could deliver a volumetric power density of 0.08 W L^{-1} and an energy density of 3.86 Wh L^{-1}. As for the 1:3 SF:IL battery, it could deliver a volumetric power density of 0.11 W L^{-1} and an energy density of 3.89 Wh L^{-1}. The 1:1 SF:IL and 1:3 SF:IL batteries demonstrated capacities of 0.96 and 0.72 mAh cm^{-2}, respectively, at a current density of 25 μA cm^{-2}. The power delivered by the 1:1 SF:IL PE battery at 8.97 μW cm^{-2} and the 1:3 SF:IL PE battery at 12.05 μW cm^{-2} fulfill the requirements for the average consumption of published implantable biomedical devices.[115,116]

Comparing the results of experiments with the Mg-air batteries and Zn-air batteries, the effects the SF:IL PE can be observed for each of the batteries. For the Mg-air batteries, the 1:1 SF:IL PE battery provided greater power and energy density when compared to the 1:3 SF:IL PE battery. However, the opposite is true when the Mg AZ31 anode material is swapped for Zn. Furthermore, the 1:3 SF:IL from the Zn-air battery displayed a different discharge profile to that of the 1:3 SF:IL Mg-air battery which suggests that the ionic liquid content of the materials impacts the discharge performance for each battery subtly differently (likely also water), implying the choline nitrate IL increases the rate of discharge and/or corrosion rate of the Mg anode material for Mg-air batteries, which is less apparent for the Zn-air batteries. To further investigate and evaluate the performance of the 1:1 and 1:3 SF:IL PEs utilized in the Zn-air batteries, the averaged (from three repeated experiments) discharge performance of the batteries with varying current applied was recorded and reported in Figure 3B. From Figure 3B the performance of each battery with 1:1 SF:IL or 1:3 SF:IL as electrolyte was observed to be similar within the current range of 20 to 100 μA in the timeframe of ca. 11 hours. However, when each battery experiences a low current of 5 and 10 μA, the 1:3 SF:IL PE battery retains a noticeably higher potential versus the 1:1 SF:IL PE battery. This observation was less pronounced when the anode material was Mg AZ31. In addition, after the batteries experienced 100 μA and then had the current reduced back to 5 μA, both the 1:1 SF:IL and 1:3 SF:IL batteries demonstrated these oscillating signals which persisted for ca. 1 hour, the full duration of the final current application step. This was the first time we observed the 1:1 SF:IL PE battery with Zn anode displaying these oscillating signals, therefore, we conclude it may be possible for the current application to affect the discharge performance of the primary Zn-air battery. As a result, from the experiments using Mg AZ31 and Zn foil as an anode material we can conclude Mg AZ31 would likely be most suitable over the current range of 5 to 100 μA due to its apparent stability and superior power offered. However, the Zn batteries did possess higher capacities, although, this did not seem to provide many benefits, possibly due to the interfering chemistries (e.g., HER) impacting the primary Zn-air batteries more than the Mg AZ31. However, the appearance of the Mg AZ31 anode after experimentation was considerably blackened (Figure S13), likely caused by corrosion of the Mg material which could suggest why the Mg batteries possessed lower capacities during the discharge performance experiments.

Finally, the ionic conductivity of the PE films post-discharge was investigated in order to compare them with the initial PEIS spectra to further showcase the stability of the PE films assembled within the batteries. The averaged Nyquist plot for the batteries utilizing the 1:1 SF:IL and 1:3 SF:IL composite films post-discharge are shown in Figure 3C. The ionic conductivity of the PE composites was estimated using Equation (1) and the data from Figure 3C, the average ionic conductivity post-discharge for the 1:1 PE film is 3.03 mS cm^{-1} and for the 1:3 PE film it is 4.55 mS cm^{-1}. Comparing the ionic conductivity of the PE composite films before and after electrochemical experimentation, the 1:1 SF:IL PE ionic conductivity is less by a factor of 1.11, whereas the 1:3 SF:IL PE ionic conductivity is less by a factor of 1.75. As a result, with the ionic conductivity of the 1:3 SF:IL PE decreasing more than the 1:1 SF:IL PE, supports the previous statement that the 1:3 SF:IL PE composite is less stable under the same experimental conditions and that with higher ionic liquid content present, the discharge performance of each battery (Mg and Zn) is impacted differently. For instance, the ionic conductivity of the 1:3 SF:IL PE assembled in the Zn anode battery decreased by more than that of the 1:3 SF:IL PE assembled in the Mg anode battery, reduction factor of 1.75

compared to pre-discharge for Zn batteries and 1.38 compared to pre-discharge for the Mg batteries. In addition, the anion (the nitrate) from the PE may also participate in the reaction with the anodes forming Mg nitrate or Zn nitrate, respectively, resulting in decreased conductivity after discharge.

The electrochemical tests using different anode materials and electrolytes highlight that when using 1:1 SF:IL PE, the performance of the batteries and stability of the films (retention of ionic conductivity after discharging) are similar with respect to their outcomes. Interestingly, when the IL content is increased in the SF films, we see the performance of the Mg and Zn batteries impacted and how exactly this is impacted seems more determined by the anode material specifically and its interactions with the constituents of the PE throughout the experiment (e.g., solvating ability of the Mg or Zn ions). Therefore, SFs role of immobilizing the IL seems vital and demonstrated to maintain the functional lifetime of the battery. As seen from Figure 3A, oscillating signals are observed ca. 35 hours. into the 1:3 SF:IL discharge experiment when using Zn as the anode. However, this was not observed for the Mg anode battery experiments (Figure 2A,B) and only observed for the 1:1 SF:IL Zn anode batteries after 100 μA current was applied (Figure 3B). Therefore, it is anticipated that the tailoring of silk composites utilized for energy storage devices can further modulate the discharge performance of batteries and lead to enhanced TIMB applications.

2.4 | Sustainability

The safety data sheets for the starting materials show nitric acid to be a corrosive oxidizer and that is toxic by inhalation, and choline hydroxide is corrosive, the corrosive nature of the two substances will be mitigated upon neutralization. *In silico* toxicity screening studies of the ionic components of the product ($[Ch]^+[NO_3]^-$) using Derek Nexus (Derek Nexus: 6.0.1, Nexus: 2.2.2)[117–120] indicate that choline is a plausible irritant for eyes and skin for humans/mammals, whereas nitrate is a plausible carcinogen in mammals (particularly when converted to nitrosamines) and plausibly toxic to the thyroid of humans/mammals, supported by the literature. *In silico* mutagenicity screening studies using Derek Nexus and Sarah Nexus (Sarah Nexus: 3.0.0, Sarah Model: 2.0) indicate both $[Ch]^+$ and $[NO_3]^-$ are non-mutagenic. With a view to the end of life of the batteries, there are dietary sources of both species ($[Ch]^+[NO_3]^-$) in human/mammalian diets,[121–124] Mg/Zn are earth abundant, and silk is a biodegradable protein,[8] consequently we expect these would be safe (within reasonable limits) for environmental/medical applications.

3 | CONCLUSION

Primary Mg-air and Zn-air batteries utilizing a SF:IL-based film as PE were studied. A variety of techniques were used to study the systems, including: Fourier-transform infrared (FTIR) spectroscopy, X-ray diffraction (XRD), thermogravimetric analysis (TGA), potentiostatic electrical impedance spectroscopy (PEIS), and galvanostatic discharge performances. The experiments undertaken showcase the batteries' performance capabilities, observing ionic conductivity of the films sufficient to satisfy the requirements for many battery applications, open circuit voltages of 1.2–1.8 V, and capacities of ca. 0.6–1 mAh cm^{-2}, dependent on the chemistry of the battery (the Mg-air batteries appeared more reliable). Future iterations of the batteries substitution of the carbon cloth, and use of degradable polymer-based cases housing the electrochemical components would result in completely transient devices. Nevertheless, more research and development in the materials science and engineering of such complex multi-component interfaces will underpin their successful translation to real-world applications, particularly electronics,[3,30,125–131] wherein there are significant opportunities employing computational approaches to advance the pace of development.[132–135]

4 | EXPERIMENTAL SECTION

Unless otherwise noted, all consumables were purchased from Sigma–Aldrich, Gillingham, UK.

4.1 | Preparation of solutions of *Bombyx mori* silk fibroin

The preparation of an aqueous solution of *Bombyx mori* silk fibroin was adapted from the literature.[73] Silk fibroin (degummed fibers, throwsters waste from Etsy) was dissolved in a calcium chloride, ethanol, and water mixture (1:2:8 molar ratio). The ratio of the silk fibers and solution was 1:20 w/v. The mixture was heated using a thermal bath at 65°C while being stirred and the silk fibers completely dissolved within 1 hour. The solution was then passed through a glass frit to remove any particulates. The filtered mixture was dialyzed for 5 days against deionized water using Pur-A-Lyzer Mega dialysis tubes 3.5 kDa molecular weight cut-off (MWCO), purchased and used as received

from Sigma–Aldrich. The solution was centrifuged at 4°C at 5000 RPM for 27.5 minutes, twice. The aqueous silk fibroin solution underwent up-concentration via dialysis (3.5 kDa MWCO) against a solution of 10% w/v PEG 10k Mw in deionized water for 48 hours. Dry weight analysis using 500 µL samples of the up-concentrated aqueous silk fibroin solution was undertaken (ca. 7 wt.% silk fibroin content), agreeing with literature values.[73]

4.2 | Preparation of the ionic liquid choline nitrate

The preparation of the ionic liquid (choline nitrate, [Ch][NO_3]) was adapted from the literature.[74] Choline-based ILs are generally prepared by the neutralization reaction of the corresponding acid with choline hydroxide.[74] [Ch][NO_3] was prepared by the neutralization reaction of nitric acid (70%) with choline hydroxide (46% wt. in water): 25 mL of choline hydroxide (46% wt. in water) was added dropwise into 6.5 mL of nitric acid (70%) in an ice bath. The reaction solution was stirred at room temperature for 24 hours. The solvent was removed by distillation and the product was vacuum dried at room temperature for 24 hours. A deep yellow-orange solution of [Ch][NO_3] was obtained with ca. 98% yield.

4.3 | Preparation of polymer electrolyte films based on silk fibroin and an ionic liquid

The preparation of the polymer electrolyte film based on silk fibroin and an ionic liquid was adapted from the literature.[59] The polymer electrolyte films were prepared by adding the [Ch][NO_3] IL into the ca. 7% SF solution with weight ratios of 1:1 and 1:3 (SF to IL). The mixtures were stirred continuously for 4 hours and 0.1 mL samples were drop cast onto a Teflon mold, followed by drying in air for 24 hours. The films had an average film thickness of ca. 0.05 cm and surface area of ca. 0.79 cm^2.

4.4 | Fourier-transform infrared (FTIR) spectroscopy

Fourier-transform infrared (FTIR) spectra were recorded in attenuate total reflectance mode on an Agilent Technologies Cary 630 FTIR from 500 to 4000 cm^{-1}, at a resolution of 4 cm^{-1}. Lint free tissue was wet with methanol and used to clean the crystal lens before each test. Data are presented in Figures S1–S4.

4.5 | X-ray diffraction (XRD)

X-ray diffraction (XRD) patterns of samples loaded onto an off-cut piece of Si(911) single crystal wafer were recorded. The samples were mounted on a Rigaku SmartLab 9 kW diffractometer equipped with a germanium (Ge) (220) 2-bounce monochromator using a parallel beam geometry, and a D/teX 250 Ultra 1D detector. The samples were analyzed by a $\theta/2\text{-}\theta$ scan with a step size of 0.01°, and a scanning rate of 3° min^{-1}. Data are presented in Figure S5.

4.6 | Thermogravimetric analysis (TGA)

Thermogravimetric analysis (TGA) was carried out using a NETZSCH STA 449 F3 TGA under a nitrogen atmosphere within the temperature range of 20 to 400°C at a heating rate of 5°C min^{-1}. Data are presented in Figure S6.

4.7 | Preparation of the Mg-air and Zn-air primary batteries

The preparation of the primary batteries was adapted from the literature.[59] The battery construction/design used in this study is shown in Figures S7–S9. The batteries utilize a 3-D printed casing, generated from a computer aided design (CAD) package (CAD Fusion 360), and printed via stereolithography (SLA). SLA of the casing was conducted using the SLA-type 3-D printer from FormLabs with the clear resin V2 at a print layer resolution of 50 µm. This casing was employed to mechanically stabilize and protect the battery and ensure there was appropriate contact between the working components within the battery casing. A Mg alloy foil, 96% Mg (Mg), 3% aluminum (Al), and 1% Zn (Zn) (AZ31) was purchased from GoodFellow with a foil thickness of 0.05 cm. The alloy's surface was polished before application by using a coarse (50) grit sandpaper followed by a fine (120) grit sandpaper and subsequently used as the anode. The geometric contact surface area of the anode assembled within the Mg air battery was calculated to be 0.79 cm^2. A Zn (Zn) 99.994% foil was purchased from Alfa Aesar with a foil thickness of 0.025 cm and was polished, as mentioned previously, before application and subsequently used as an alternative anode. The geometric contact surface area of the alternative anode assembled within the Zn air battery was also calculated to be 0.79 cm^2. A 2 mg cm^{-2} platinum (Pt) black carbon cloth electrode was purchased from FuelCellStore with a cloth thickness of 0.0365 cm and used as the cathode for the ORR and the geometric contact surface area of the cathode assembled within the batteries was calculated to be 0.79 cm^2. The PEs

1:1 and 1:3 SF:IL composite films were assembled inside independent batteries using Mg AZ31 alloy foil or Zn foil as the anode.

4.8 | Potentiostatic electrical impedance spectroscopy (PEIS)

The pre-discharge ionic conductivity of the PE 1:1 and 1:3 composite films assembled in the final batteries (two-electrode electrochemical cell) were deduced by conducting PEIS using a Biologic SP-300 potentiostat, with an alternating current (AC) with an amplitude of 10 mV with the frequency range set at 100,000 to 0.1 Hz, open circuit potential (OCP). The ionic conductivity of the films was estimated using Equation (1):

$$\sigma = d/RA \tag{1}$$

where σ is the conductivity (S cm^{-1}), d the thickness of the film (cm), R is the bulk resistance (Ω) obtained from the first intercept on the x-axis of the complex plane, and A is the contact area (cm^2).[74,104,106] Where the measurements never intercepts the x-axis, the R values were approximated via extrapolation as they are not likely to deviate much from a linear slope for the missing datapoints.

4.9 | Battery performances

The galvanostatic discharge performance of the batteries (two-electrode electrochemical cell) was evaluated using a Biologic SP-300 potentiostat. The experiments involved two different techniques while the open circuit potential (OCP) was measured for the first 10 minutes beforehand to ensure that the batteries were operating as expected. The first technique utilized was a continuous discharge with a constant current of 20 μA being applied and proceeded until the minimum voltage cut-off (0 V) was reached. The second technique utilized was an increasing current discharge with each new current applied persisting for 1 hour before the next. The experiment began with 5 μA current being applied, then increased to 10 μA after 1 hour, then 20 μA, then increments of 10 μA until 80 μA was reached, then 100 μA and finally having the current applied reduced back to 5 μA for the final 1 hour. The post-discharge ionic conductivity of the PE 1:1 and 1:3 composite films assembled in the batteries (two-electrode electrochemical cell) were deduced by conducting PEIS using Biologic SP-300 potentiostat, with an amplitude of 10 mV with the frequency range set at 100,000 to 0.1 Hz, OCP. The specific volumetric power density (P) of the batteries was calculated from the discharge curves using the Equation (2):

$$P = UI/V \tag{2}$$

where P is the volumetric power density (W L^{-1}), U is the plateau voltage (V) of the discharge curve, I is the discharge current (A), and V is the working device volume (L).[1] The V of the SF:IL Mg-air battery is 1.065×10^{-4} L, whereas the V of the SF:IL Zn-air battery is 8.697×10^{-5} L.

4.10 | In silico toxicity screening

In silico toxicity, screening was carried out using Derek Nexus (v. 6.0.1, Nexus: 2.2.2) and Sarah Nexus (Sarah Nexus: 3.0.0, Sarah Model: 2.0) supplied by Lhasa Ltd., Leeds, UK.[117–120] The simplified molecular-input line-entry system (SMILES) notation for choline is: C[N+](C)(C)CCO, and for nitrate is: [N+]([O−])([O−])=O.

ACKNOWLEDGMENTS

The manuscript was written through contributions of all authors. All authors have given approval to the final version of the manuscript. We thank Garry R. Harper and Vasileios K. Oikonomou for insightful discussions about silk processing during the preliminary stage of the project, and Dhruv Trivedi for insightful discussions about batteries throughout the project. We acknowledge the financial support for M.J.H. from the UKRI Engineering and Physical Sciences Research Council (EPSRC) DTP PhD Studentship (Grant reference: EP/R513076/1, 2145109). J.G.H. acknowledges support from the Royal Society (RG160449). We thank the Ministry of Education of Saudi Arabia and the Saudi Cultural Bureau for financial support for H.A.G. (Grant: KAU1526). Supporting Information is available from the Wiley Online Library or from the author.

CONFLICT OF INTEREST

The authors declare no conflict of interest.

DATA AVAILABILITY STATEMENT

The data that support the findings of this study are available from the corresponding author upon reasonable request.

REFERENCES

1. World Economic Forum, A New Circular Vision for Electronics, Time for a Global Reboot, https://www.weforum.org/reports/a-new-circular-vision-for-electronics-time-for-a-global-reboot, (Accessed 2nd June 2022).

2. A. Stowell, J. Hardy, N. Cass, H. Stewart, *Zenodo* **2020**, 1–24. https://doi.org/10.5281/zenodo.4058351, (Accessed 2nd June 2022).
3. S. Rarotra, S. Sahu, P. Kumar, K. H. Kim, Y. F. Tsang, V. Kumar, P. Kumar, M. Srinivasan, A. Veksha, G. Lisak, *ChemistrySelect* **2020**, *5*(20), 6182–6193.
4. G. Iaquaniello, G. Centi, A. Salladini, E. Palo, S. Perathoner, *Chem. Eur. J.* **2018**, *24*(46), 11831–11839.
5. M. Kahl, S. Pavón, M. Bertau, *Chem. Phys. Chem* **2021**, *22*(6), 577–584.
6. United Nations, Department of Economic and Social Affairs Sustainable Development, https://sdgs.un.org/goals, (Accessed 2nd June 2022).
7. S. Sthiannopkao, M. H. Wong, *Sci. Total Environ.* **2013**, *463–464*, 1147–1153.
8. C. Tulkoff, G. Caswell, *Design for Excellence in Electronics Manufacturing*, Wiley, Weinheim, **2021**.
9. M. Kirschner, *Adv. Sustain. Syst.* **2022**, *6*(2), 1–5.
10. S. Dühnen, J. Betz, M. Kolek, R. Schmuch, M. Winter, T. Placke, *Small Methods* **2020**, *4*(7), 1–38.
11. M. P. Bracciale, *Sustainable Strateg. Org. Electron.* **2022**, 507–519.
12. J. Ma, *Battery Technologies: Materials and Components*, Wiley-VCH, Weinheim, **2022**.
13. S. Passerini, D. Bresser, A. Moretti, A. Varzi, *Batteries: Present and Future Energy Storage Challenges*, Wiley-VCH, Weinheim, **2020**.
14. U. Datta, A. Kalam, J. Shi, *Energy Storage*, **2021**, *3*(5), 1–21.
15. L. A. Wehner, N. Mittal, T. Liu, M. Niederberger, *ACS Cent. Sci.* **2021**, *7*, 2, 231–244.
16. Q. Liu, Z. Chang, Z. Li, X. Zhang, *Small Methods* **2018**, *2*(2), 1–16.
17. F. Tong, X. Chen, Q. Wing, S. Wei, W. Gao, *J. Alloys Compd.* **2021**, 1–10.
18. F. Bella, S. De Luca, L. Fagiolari, D. Versaci, J. Amici, C. Francia, S. Bodoardo, *Nanomaterials* **2021**, *11*(810), 1–29.
19. T. Zhang, Z. Tao, J. Chen, *Mater. Horizons* **2014**, *1*, 196–206.
20. A. Hahn, J. P. Schuchardt, *Curr. Nutrit. Food Sci.* **2017**, *13*, 260–278.
21. W. Du, E. H. Ang, Y. Yang, Y. Zhang, M. Ye, C. C. Li, *Energy Environ. Sci.* **2020**, *13*, 3330–3360.
22. M. B. Kannan, C. Moore, S. Saptarshi, S. Somasundaram, M. Rahuma, A. L. Lopata, *Sci. Rep.* **2017**, *7*, 1–11.
23. J. J. D. Venezuela, S. Johnston, M. S. Dargusch, *Adv. Healthcare Mater.* **2019**, *8*, 1–15.
24. Z. Zhao, X. Fan, J. Ding, W. Hu, C. Zhong, J. Lu, *ACS Energy Lett*. **2019**, *4*, 2259–2270.
25. S. W. Hwang, John A. Rogers, *Green Mater. Electron.* **2017**, 146–160.
26. W. B. Han, J. H. Lee, J. W. Shin, S. W. Hwang, *Adv. Mater.* **2020**, *32*(51), 1–17.
27. R. Jamshidi, M. Taghavimehr, Y. Chen, N. Hashemi, R. Montazami, *Adv. Sustain. Syst.* **2021**, *6*(2), 1–13.
28. J. S. Shim, J. A. Rogers, S. K. Kang, *Mater. Sci. Eng. R.* **2021**, 1–41.
29. L. Yin, H. Cheng, S. Mao, R. Haasch, Y. Liu, X. Xie, S. W. Hwang, H. Jain, S. K. Kang, Y. Su, R. Li, Y. Huang, John A. Rogers, *Adv. Funct. Mater.* **2014**, *24*(5), 645–658.
30. C. Liedel, *ChemSusChem* **2020**, *13*(9), 2110–2141.
31. B. Kılıçarslan, I. Bozyel, D. Gökcen, C. Bayram, *Macromol. Mater. Eng.* **2022**, *307*(6), 1–28.
32. A. Uva, A. Lin, J. Babi, H. Tran, *J. Chem. Technol. Biotechnol.* **2022**, *97*(4), 801–809.
33. H. Tran, V. R. Feig, K. Liu, H. C. Wu, R. Chen, J. Xu, K. Deisseroth, Z. Bao, *ACS Cent. Sci.* **2019**, *5*, 1884–1891.
34. J. A. Chiong, H. Tran, Y. Lin, Y. Zheng, Z. Bao, *Adv. Sci.* **2021**, *8*(14), 1–30.
35. J. Liu, H. Yuan, X. Tao, Y. Liang, S. J. Yang, J. Q. Huang, T. Q. Yuan, M. M. Titirici, Q. Zhang, *EcoMat Funct. Mater. Green Energy Environ.* **2020**, *2*(1), 1–16.
36. C. J. Bettinger, Z. Bao, *Polym. Int.* **2010**, *59*(5), 563–567.
37. D. Gao, J. Lv, P. S. Lee, *Adv. Mater.* **2022**, *34*(25), 1–16.
38. M. Bolognesi, M. Prosa, M. Seri, *Sustainable Strateg. Org. Electron.* **2022**, 297–338.
39. L. Yin, X. Huang, H. Xu, Y. Zhang, J. Lam, J. Cheng, J. A. Rogers, *Adv. Mater.* **2014**, *26*(23), 3879–3884.
40. J. P. Esquivel, P. Alday, O. A. Ibrahim, B. Fernández, E. Kjeang, N. Sabaté, *Adv. Energy Mater.* **2017**, *7*(18), 1–11.
41. M. H. Lee, J. Lee, S. K. Jung, D. Kang, M. S. Park, G. D. Cha, K. W. Cho, J. H. Song, S. Moon, Y. S. Yun, S. J. Kim, Y. W. Lim, D. H. Kim, K. Kang, *Adv. Mater.* **2011**, *33*(10), 1–11.
42. G. Lee, S. K. Kang, S. M. Won, P. Gutruf, Y. R. Jeong, J. Koo, S. S. Lee, J. A. Rogers, J. S. Ha, *Adv. Energy Mater.* **2017**, *7*(18), 1–12.
43. N. P. Balsara, D. T. Hallinan, *Annu. Rev. Mater. Res.* **2013**, *43*, 503–525.
44. A. Manthiram, X. Yu, S. Wang, *Nat. Rev. Mater.* **2017**, *2*, 16103.
45. P. M. Vereecken, X. Chen, *Adv. Mater. Interfaces* **2019**, *6*, 1–31.
46. T. P. Nguyen, A. D. Easley, N. Kang, S. Khan, S. M. Lim, Y. H. Rezenom, S. Wang, D. K. Tran, J. Fan, R. A. Letteri, X. He, L. Su, C. H. Yu, J. L. Lutkenhaus, K. L. Wooley, *Nature* **2021**, *593*, 61–66.
47. M. Wu, Y. Zhang, L. Xu, C. Yang, M. Hong, M. Cui, B. C. Clifford, S. He, S. Jing, Y. Yao, L. Hu, *Matter* **2022**, *5*(10), 3402–3416.
48. N. Delaporte, G. Lajoie, S. Collin-Martin, K. Zaghib, *Sci. Rep.* **2020**, *10*(3812), 1–18.
49. X. Aeby, A. Poulin, G. Siqueira, M. K. Hausmann, G. Nyström, *Adv. Mater.* **2021**, *33*, 1–9.
50. D. She, M. Tsang, J. K. Kim, M. G. Allen, *Actuators Microsystems* **2015**, 494–497.
51. M. Karami-Mosammam, D. Danninger, D. Schiller, M. Kaltenbrunner, *Adv. Mater.* **2022**, *34*, 1–11.
52. Z. Liu, P. Bertram, F. Endres, *J. Solid State Electrochem. 21*, **2017**, 2021–2027.
53. Z. Liu, G. Pulletikurthi, F. Endres, *ACS Appl. Mater. Interfaces* **2016**, *8*, 12158–12164.
54. A. Chiappone, C. Gerbaldi, I. Roppolo, N. Garino, R. Bongiovanni, *Polymer* **2015**, *75*, 64–72.
55. L. Liu, S. Yu, Y. Niu, E. Liu, *J. Alloys Compd.* **2020**, *835*, 1–13.
56. X. Ou, Q. Liu, J. Pan, L. Li, Y. Hu, Y. Zhou, F. Yan, *Chem. Eng. J.*, **2022**, *435*, 1–8.
57. R. Xu, J. Zhou, H. Gong, L. Qiao, Y. Li, D. Li, M. Gao, G. Xu, M. Wang, X. Liang, X. Zhang, M. Luo, H. Qiu, K. Liang, Y. Li, *Biomaterials Sci.* **2022**, *10*, 1476–1485.
58. J. C. Barbosa, A. Reizabal, D. M. Correia, A. Fidalgo-Marijuan, R. Gonçalves, M. M. Silva, S. Lanceros-Mendez, C. M. Costa, *Mater. Today Energy* **2020**, *18*, 1–10.
59. X. Jia, C. Wang, V. Ranganathan, B. Napoer, C. Yu, Y. Chao, M. Forsyth, F. G. Omenetto, D. R. MacFarlane, G. G. Wallace, *ACS Energy Lett.* **2017**, *2*, 831–836.

60. S. Aznar-Cervantes, M. I. Roca, J. G. Martinez, L. Meseguer-Olmo, J. L. Cenis, J. M. Moraleda, T. F. Otero, *Bioelectrochemistry* **2012**, *85*, 36–43.
61. J. G. Hardy, L. M. Romer, T. R. Scheibel, *Polymer* **2008**, *49*, 4309–4327.
62. J. G. Hardy, T. R. Scheibel, *Progress in Polymer Sci*. **2010**, *35*, 1093–1115.
63. C. Vepari, D. L. Kaplan, *Progress in Polymer Sci*. **2007**, *32*, 991–1007.
64. Y. Qi, H. Wang, K. Wei, Y. Yang, R. Zheng, I. S. Kim, K. Zhang, *Mol. Sci.* **2017**, *18*, 1–15.
65. C. Holland, K. Numata, J. Rnjak-Kovacina, F. P. Seib, *Adv. Healthcare Mater.* **2019**, *8*, 1–22.
66. A. Veronica, I. Hsing, *ChemPhysChem* **2021**, *22*(22), 2266–2280.
67. C. Lee, S. Kim, Y. H. Cho, *Adv. Sustainable Syst.* **2022**, *6*(2), 1–34.
68. S. Strassburg, S. Zainuddin, T. Scheibel, *Adv. Energy Mater.* **2021**, *11*, 2100519, 1–19.
69. R. Wu, L. Ma, X. Y. Liu, *Adv. Sci.* **2022**, *9*, 2103989, 1–25.
70. B. Zhu, H. Wang, W. R. Leow, Y. Cai, X. J. Loh, M. Y. Han, X. Chen, *Adv.Mater*. **2016**, *28*, 4250–4265.
71. P. F. Ng, J. Hua, C. Liu, Y. Wang, R. Yin, B. Fei, *ACS Materials Lett*. **2020**, *2*, 7, 801–807.
72. N. Syazana, M. Yusoff, M. U. Wahit, J. Jaafar, T. W. Wong, *Mater. Today Proc. 5*, **2018**, 21853–21860.
73. S. T. Mousavi, G. R. Harper, S. Municoy, M. D. Ashton, D. Townsend, G. H. K. Alsharif, V. K. Oikonomou, M. Firlak, S. Au-Yong, B. E. Murdock, G. R. Akien, N. R. Halcovitch, S. J. Baldock, M. Fazilati, O. V. Kolosov, B. J. Robinson, M. F. Desimone, J. G. Hardy, *Macromol. Mater. Eng.* **2020**, *305*, 2000130, 1–7.
74. X. Jia, Y. Yang, C. Wang, C. Zhao, R. Vijayaraghavan, D. R. MacFarlane, M. Forsyth, G. G. Wallace, *ACS Appl. Mater. Interfaces* **2014**, *6*, 21110–21117.
75. M. Southcott, K. MacVittie, J. Halamek, L. Halamkova, W. D. Jemison, R. Lobel, E. A. Katz, *Phys. Chem. Chem. Phys.* **2013**, *15*, 6278–6283.
76. E. Jonsson, *Energy Storage Mater.* **2020**, *25*, 827–835.
77. W. Zhou, M. Zhang, X. Kong, W. Huang, Q. Zhang, *Adv. Sci.* **2021**, *8*, 1–21.
78. N. Zhu, K. Zhang, F. Wu, Y. Bai, C. Wu, *Energy Mater. Adv.* **2021**, 1–29.
79. T. Yamamoto, R. Matsubara, T. Nohira, *J. Chem. Eng. Data*. **2021**, *66*(2), 1081–1088.
80. H. Qi, Y. Ren, S. Guo, Y. Wang, S. Li, Y. Hu, F. Yan, *ACS Appl. Mater. Interfaces* **2020**, *12*(1), 591–600.
81. G. T. Kim, S. S. Jeong, M. Joost, E. Rocca, M. Winter, S. Passerini, A. Balducci, *J. Power Sources* **2011**, *196*, 2187–2194.
82. S. K. Shukla, J. Mikkola, *Front. Chem.* **2020**, *8*, 1–23.
83. A. Schindl, M. L. Hagen, S. Muzammal, H. A. D. Gunasekera, A. K. Croft, *Front. Chem.* **2019**, *7*, 1–31.
84. L. Bui-Le, C. J. Clarke, A. Bröhl, A. P. S. Brogan, J. A. J. Arpino, K. M. Polizzi, J. P. Hallett, *Communications Chemistry*, **2020**, *3*(55), 1–9.
85. A. Kumar, K. Bhakunia, P. Venkatesu, *Phys. Chem. Chem. Phys.* **2019**, *21*, 23269–23282.
86. H. Weingärtner, C. Cabrele, C. Herrmann, *Phys. Chem. Chem. Phys.* **2012**, *14*, 415–426.
87. C. Schröder, *Top. Curr. Chem.* **2017**, *375*, 1–26.
88. L. Gontrani, *Biophys. Rev.* **2018**, *10*, 873–880.
89. B. L. Gadilohar, G. S. Shankarling, *J. Mol. Liq.* **2017**, *227*, 234–261.
90. E. E. L. Tanner, K. M. Piston, H. Ma, K. N. Ibsen, S. Nangia, S. Mitragotri, *Biomaterials Sci. Eng.* **2019**, *5*(7), 3645–3653.
91. D. M. Phillips, L. F. Drummy, D. G. Conrady, D. M. Fox, R. R. Naik, M. O. Stone, P. C. Trulove, H. C. D. Long, A R, *J. Am. Chem. Soc.* **2004**, *126*(44), 14350–14351.
92. H. Heng, Q. Deng, Y. Yang, F. Wang, *Int. J. Mol. Sci.* **2022**, *23*(15), 1–21.
93. A. A. Lozano-Pérez, M. G. Montalbán, S. D. Aznar-Cervantes, F. Cragnolini, J. L. Cenis, G. Víllora, *Appl. Polymer Sci.* **2015**, *132*(12), 1–8.
94. R. F. P. Pereira, K. Zehbe, C. Günter, T. dos Santos, S. C. Nunes, F. A. Almeida Paz, M. M. Silva, P. L. Granja, A. Taubert, V. de Zea Bermudez, *ACS Omega*, **2018**, *3*(9), 10811–10822.
95. I. P. Moreira, C. Esteves, S. I. C. J. Palma, E. Ramou, A. L.M. Carvalho, A. C. A. Roque, *Mater.Today Bio*. **2022**, *15*, 109.
96. N. Goujon, X. Wang, R. Rajkowa, N. Byrne, *Chem. Commun.* **2012**, *48*, 1278–1280.
97. O. A. El Seoud, M. Kostag, S. Possidonio, M. T. Dignani, P. A. R. Pires, M. C. Lourenço, *Polymers* **2022**, *14*(13), 1–16.
98. T. C. D. Fernandes, H. M. R. Rodrigues, F. A. A. Paz, J. F. M. Sousa, A. J. M. Valente, M. M. Silva, V. de Zea Bermudez, R. F. P. Pereira, *J. Electrochem. Soc.* **2020**, *167*, 1–11.
99. A. R. P. Gonçalves, X. Paredes, A. F. Cristino, F. J. V. Santos, C. S. G. P. Queirós, *Int. J. Mol. Sci.* **2021**, *22*, 1–50.
100. R. F. P. Pereira, R. Brito-Pereira, R. Goncalves, M. P. Silva, C. M. Costa, M. Manuela Silva, V. de Zea Bermudez, S. Lanceros-Mendez, *ACS Appl. Mater. Interfaces* **2018**, *10*, 5385–5394.
101. L. Yu, G. Z. Chen, *Front. Chem.* **2019**, *7*, 1–15.
102. W. Wang, Y. Liu, S. Wang, X. Fu, T. Zhao, X. Chen, Z. Shao, *ACS Appl. Mater. Interfaces* **2020**, *12*(22), 25353–25362.
103. S. Yamada, *ChemRxiv* **2022**, 1–32.
104. T. Monetta, A. Carangelo, A. Acquesta, *J. Magnesium Alloys* **2019**, *7*(2), 218–226.
105. M. Samie, N. Muhammad, M. A. Yameen, A. A. Chaudhry, H. Khalid, A. F. Khan, *J. Polym. Environ.* **2020**, *28*, 657–667.
106. H. Zhang, L. L. Li, F. Y. Dai, H. H. Zhang, B. Ni, W. Zhou, X. Yang, Y. Z. Wu, *J. Transl. Med.* **2012**, *10*(117), 1–9.
107. M. Boulet-Audet, F. Vollrath, C. Holland, *J. Experimental Bio.* **2015**, *218*, 3138–3149.
108. T. Yamane, K. Umemura, Y. Nakazawa, T. Asakura, *Macromolecules* **2003**, *36*, 6766–6772.
109. Q. Lu, X. Hu, X. Wang, J. A. Kluge, S. Lu, P. Cebe, D. L. Kaplan, *Acta Biomater*. **2010**, *6*, 1380–1387.
110. N. Jaramillo-Quicenoa, C. Alvarez-Lopez, A. Restrepo-Osorio, *Proc. Eng*. **2017**, *200*, 384–388.
111. M. Agostini de Moraes, G. M. Nogueira, R. F. Weska, M. M. Beppu, *Polymers* **2010**, *2*, 719–727.
112. S. Ha, A. E. Tonelli, S. M. Hudson, *Biomacromolecules* **2005**, *6*, 3, 1722–1731.
113. M. J. Haskew, B. Deacon, C. W. Yong, J. G. Hardy, S. T. Murphy, *ACS Omega* **2021**, *6*, 35494–35504.
114. B. Marelli, M. A. Brenckle, D. L. Kaplan, F. G. Omenetto, *Sci. Rep.* **2016**, *6*, 25263.
115. E. Sejdic, K. Bocan, *Sensors* **2016**, *16*(3), 1–23.
116. K. D. Weaver, H. J. Kim, J. Sun, D. R. MacFarlane, G. D. Elliott, *Green Chem*. **2010**, *12*, 507–513.

117. C. Barber, A. Cayley, T. Hanser, A. Harding, C. Heghes, J. D. Vessey, S. Werner, S. K. Weiner, J. Wichard, A. Giddings, S. Glowienke, A. Parenty, A. Brigo, H. Spirkl, A. Amberg, R. Kemper, N. Greene, *Regul. Toxicol. Pharm.* **2016**, *76*, 7–20.
118. D. S. Macmillan, M. L. Chilton, *Regul. Toxicol. Pharm.*, **2019**, *101*, 35–37.
119. N. Greene, P. N. Judson, J. J. Langowski, C. A. Marchant, *SAR QSAR Environ Res.* **1999**, *10*(2-3), 299–314.
120. Lhasa Limited, www.lhasalimited.org, (Accessed 29th April 2022).
121. S. Sekar, M. Surianarayanan, V. Ranganathan, D. R. MacFarlane, A. B. Manda, *Environ. Sci. Technol.* **2012**, *46*, 4902–4908.
122. S. H. Zeisel, *Ann, Rev. Nutr.* **1994**, *14*, 269–296.
123. A. M. A. Dias, A. R. Cortez, M. M. Barsan, J. B. Santos, C. M. A. Brett, H. C. Sousa, *ACS Sustainable Chem. Eng.* **2013**, *1*, 1480–1492.
124. O. Winther-Jensen, R. Vijayaraghavan, J. Sun, B. Winther-Jensen, D. R. MacFarlane, *Chem. Commun.* **2009**, 3041–3043.
125. N. Koch, *ChemPhysChem*, **2007**, *8*(10), 1438–1455.
126. S. W. Hwang, H. Tao, D. H. Kim, H. Cheng, J. K. Song, E. Rill, M. A. Brenckle, B. Panilaitis, S. M. Won, Y. S. Kim, Y. M. Song, K. J. Yu, A. Ameen, R. Li, Y. Su, M. Yang, D. L. Kaplan, M. R. Zakin, M. J. Slepian, Y. Huang, F. G. Omenetto, J. A. Rogers, *Science* **2012**, *337*(6102), 1640–1644.
127. W. B. Han, S. M. Yang, K. Rajaram, S. W. Hwang, *Adv. Sustainable Sys.* **2021**, *6*(2), 1–17.
128. X. Yu, A. Manthiram, *Adv. Energy Sustainability Res.* **2021**, *2*(5), 1–12.
129. J. Popovic, *Macromol. Chem. Phys.* **2022**, *223*(8), 1–11.
130. G. Jiang, L. Liu, J. Xiong, Y. Luo, L. Cai, Y. Qian, H. Wang, L. Mu, X. Feng, X. Lu, J. Zhu, *Macromol. Biosci.* **2022**, *22*(6), 1–16.
131. D. Mecerreyes, L. Porcarelli, N. Casado, *Macromol. Chem. Phys.* **2020**, *221*(4), 1–7.
132. D. Atkins, E. Ayerbe, A. Benayad, F. G. Capone, E. Capria, I. E. Castelli, I. Cekic-Laskovic, R. Ciria, L. Dudy, K. Edström, M. R. Johnson, H. Li, J. M. G. Lastra, M. L. De Souza, V. Meunier, M. Morcrette, H. Reichert, P. Simon, J. P. Rueff, J. Sottmann, W. Wenzel, A. Grimaud, *Adv. Energy Mater.* **2022**, *12*(17), 1–23.
133. E. Ayerbe, M. Berecibar, S. Clark, A. A. Franco, J. Ruhland, *Adv. Energy Mater.* **2022**, *12*(17), 1–24.
134. S. Clark, F. L. Bleken, S. Stier, E. Flores, C. W. Andersen, M. Marcinek, A. Szczesna-Chrzan, M. Gaberscek, M. R. Palacin, M. Uhrin, J. Friis, *Adv. Energy Mater.* **2022**, *12*(17), 1–26.
135. A. Bhowmik, M. Berecibar, M. Casas-Cabanas, G. Csanyi, R. Dominko, K. Hermansson, M. R. Palacin, H. S. Stein, T. Vegge, *Adv. Energy Mater.* **2022**, *12*(17), 1–20.

SUPPORTING INFORMATION

Additional supporting information can be found online in the Supporting Information section at the end of this article.

How to cite this article: M. J. Haskew, S. Nikman, C. E. O'Sullivan, H. A. Galeb, N. R. Halcovitch, J. G. Hardy, S. T. Murphy, *Nano Select*. **2022**, 1. https://doi.org/10.1002/nano.202200200